Research Article | Vol. 30, No. 8 / 11 Apr 2022 / Optics Express 12248
Optics EXPRESS

Reconstruction of ultrafast exciton dynamics with a phase-retrieval algorithm

GIAN LUCA DOLSO,[1,5] BRUNO MOIO,[1,2,5] GIACOMO INZANI,[1] NICOLA DI PALO,[1,2] SHUNSUKE A. SATO,[3,4] ROCÍO BORREGO-VARILLAS,[2] MAURO NISOLI,[1,2] AND MATTEO LUCCHINI[1,2,*]

[1]*Department of Physics, Politecnico di Milano, 20133 Milano, Italy*
[2]*Institute for Photonics and Nanotechnologies, IFN-CNR, 20133 Milano, Italy*
[3]*Center for Computational Sciences, University of Tsukuba, Tsukuba 305-8577, Japan*
[4]*Max Planck Institute for the Structure and Dynamics of Matter, 22761 Hamburg, Germany*
[5]*Equal contributors*
[*]*matteo.lucchini@polimi.it*

Abstract: The first step to gain optical control over the ultrafast processes initiated by light in solids is a correct identification of the physical mechanisms at play. Among them, exciton formation has been identified as a crucial phenomenon which deeply affects the electro-optical properties of most semiconductors and insulators of technological interest. While recent experiments based on attosecond spectroscopy techniques have demonstrated the possibility to observe the early-stage exciton dynamics, the description of the underlying exciton properties remains non-trivial. In this work we propose a new method called extended Ptychographic Iterative engine for eXcitons (ePIX), capable of reconstructing the main physical properties which determine the evolution of the quasi-particle with no prior knowledge of the exact relaxation dynamics or the pump temporal characteristics. By demonstrating its accuracy even when the exciton dynamics is comparable to the pump pulse duration, ePIX is established as a powerful approach to widen our knowledge of solid-state physics.

1. Introduction

The possibility to observe and control the ultrafast physical processes triggered by light in matter is a long-pursued goal of solid-state physics which will enable future device engineering along with the acquisition of superior performances [1]. In this respect, the identification and understanding of the electron dynamics dictating the sudden energy redistribution after optical excitation are a prerequisite to achieve control. In the last decade, Attosecond Transient Absorption/Reflection Spectroscopy (respectively ATAS and ATRS) have been established as one of the most powerful tools to investigate the ultrafast optical response of metals [2], semiconductors [3–9] and insulators [10–14]. These spectroscopic techniques take advantage of the element-specificity of extreme-ultraviolet (XUV) photons to probe the ultrafast dynamics induced by the interaction of the solid sample with a few-cycle infrared (IR) pump pulse [15]. Particular attention has been recently drawn by the study of the dynamical response of excitons, as these quasi-particles find applications in many relevant technological areas, including optoelectronics, photonics and excitonics [16–18]. Due to the relatively high photon energy of the attosecond radiation, the first pioneering experiments focused on core excitonic states, i.e. quasi-particles formed by the Coulomb interaction between an electron in the conduction band and a core hole [14,19,20].

Typically, a few-femtosecond IR pulse drives the system out of equilibrium, while the optical response is probed by the attosecond XUV radiation. Information about the exciton dynamics is encoded in a differential spectrogram, obtained by measuring the spectrum of the transmitted/reflected XUV radiation as a function of the relative delay with the IR pump pulse.

#451759 https://doi.org/10.1364/OE.451759
Journal © 2022 Received 14 Jan 2022; revised 4 Mar 2022; accepted 4 Mar 2022; published 28 Mar 2022

Optics EXPRESS

Unfortunately, it is not possible to directly access the exciton characteristics (*e.g.* its lifetime, polarizability, etc.) from the measured spectrogram. A possible approach to overcome this limitation is to fit the experimental data using a mathematical model to estimate the real-time behaviour of the core-exciton state [20]. To describe comprehensively the time-dependent excitonic dipole several fitting parameters must be considered (*i.e.*, phonon coupling, Auger decay, complex polarizability, and pump laser characteristics). Therefore, without a well-educated guess or an *a-priori* knowledge of some of the above mentioned physical parameters the fitting procedure may be ill-posed, hindering a reliable convergence.

In this work, we propose a novel approach named extended Ptychographic Iterative engine for eXcitons (ePIX), to retrieve the ultrafast dynamics of a core-exciton state from a transient reflection spectrogram. This method requires no prior information about the dynamics of the excited state and no complete characterization of the driving IR field. Moreover, since the algorithm is based on a two-level atomic model, ePIX can be used to investigate the ultrafast physical processes happening in several other systems which can be framed within this representation, like atoms and molecules [21–23]. Therefore, the proposed methodology is general and its applicability extends beyond the solid-state physics.

Our work is based on a reformulation of the Ptychographic Iterative Engine (PIE) algorithm and its extended version (ePIE) [24–26] used to characterize the light pulses involved in attosecond streaking experiments [27]. Compared to a 2D fitting procedure, we found that ePIX assures robust convergence also when no *a-priori* information on the system physical parameters is available. In addition, the ePIX retrieval procedure does not assume any functional form of the exciton dynamics and can therefore retrieve an exciton time-dependent dipole with an arbitrary shape. While this is a big advantage when the time-dependent dipole constitutes the primary object of the study, a mathematical model is still needed if one aims to extract the exciton physical parameters (e.g. Auger decay) from the dipole time evolution, thus requiring a subsequent 1D fitting procedure. However, as we will discuss in the following, applying ePIX reconstruction and a subsequent 1D fit gives a more accurate reconstruction than a global 2D fitting procedure, especially when the observed dynamics unfolds on a time scale comparable to the pump pulse duration.

The work is organized as follows. In Section 2. we present the atomic-like model that predicts the temporal evolution of the core-exciton ground state under the effect of an external electric field. Section 3. describes the implementation of the reconstruction algorithm we developed. We present the results of the reconstruction applied to a show-case simulated ATRS trace in Section 4, while the reconstruction output at each step of the algorithm is discussed in Section 5. Finally, Section 6. discusses the applicability of ePIX to experimental traces characterized by a finite noise, while Section 7. demonstrates that ePIX can be extended to consider optical traces originated by the coherent contribution of multiple excitonic transitions.

2. Core-exciton transient reflectivity contribution

In an ATAS or ATRS experiment, the attosecond radiation creates the core exciton in the presence of the external IR driving field, which perturbs the system relaxation process. On the attosecond time scale the IR field can induce solid-like phenomena like the dynamical Franz-Keldysh effect [28], which produces fast oscillations in the transient signal, related to the exciton nanometric motion [14]. The system response on the few-fs time scale is instead dominated by atomic-like effects, such as the optical Stark effect [29], which transient signature encodes information on the exciton relaxation mechanism [20]. In this work we will concentrate on the latter class of phenomena as the study of the attosecond timing of the exciton dynamics requires a different experimental and theoretical approach which goes beyond the present scope. In particular, we will model the exciton with non-dispersive localized states, whose temporal evolution is described by an exponential decay due to an Auger relaxation process plus a Gaussian decay via

Optics EXPRESS

phonon coupling [19,20,30], and concentrate only on the femtosecond dynamics. For the sake of simplicity, at first, we analyse the evolution of the exciton in its ground state, neglecting other bright or dark excited states. As we will discuss in Section 7, this does not limit the validity and generality of our approach.

If we assume the exciton formation to be instantaneous and the XUV pulse to be considerably shorter than the pump pulse, so that it can be approximated with a delta function in time, the system electrical permittivity $\epsilon(\omega, \tau)$, as a function of the XUV photon frequency ω and of the delay τ between the XUV and IR pulses, can be expressed as follows [19]:

$$\epsilon(\omega, \tau) = \epsilon_0 + k \int_{-\infty}^{+\infty} H(t)\, e^{-\frac{t}{T_e}} e^{-i\omega_e t} e^{\Phi(t)} e^{i\Psi_{IR}(t)} e^{i\omega t}\, dt \tag{1}$$

where ϵ_0 is the crystal electrical permittivity, here supposed for simplicity to be 1, k is a constant accounting for the strength of the core-exciton response, $H(t)$ is the Heaviside function describing the instantaneous exciton formation, T_e is the Auger lifetime of the excited state and $\hbar\omega_e$ is the excitation energy. A non-null ω_e is responsible for a strong linear contribution of the dipole phase which can be clearly seen in the simulations and in the reconstruction results. In the simulations the Heaviside $H(t)$ was substituted in the simulations with the complementary error function $\frac{1}{2}\,\mathrm{erfc}(-t)$, that exhibits a smoother slope. This was done to consider the more physically realistic case mimicking a finite excitation time. In a real experiment ϵ_0 can be estimated from the out-of-resonance static reflectance of the material and subtracted before reconstruction.

The function $\Phi(t)$ governs the coupling with phonons and reads:

$$\Phi(t) = -\frac{M_0^2}{\omega_0^2}\left[(2N+1)\,(1-\cos\omega_0 t) - i\,(\omega_0 t - \sin\omega_0 t)\right]. \tag{2}$$

Here, M_0 is the phonon coupling coefficient, accounting for the strength of the phonon relaxation, $\hbar\omega_0$ is the phonon energy and N is the phonon population, derived from the Boltzmann statistics. Typically, $N \ll 1$, so we set $N = 0$ in our simulations. The term Ψ_{IR}, which depends on the IR field $E(t)$, describes the optical Stark effect as follows [31,32]:

$$\Psi_{IR} = -\left(\frac{\alpha}{2} - i\gamma\right)\int_0^t E^2\,(t'-\tau)\,dt', \tag{3}$$

where $\alpha/2$ and γ represent the real and imaginary part of the polarizability of the core exciton. The lower extreme of the integral, set to zero, is equal to the XUV arrival time because the Stark effect only starts after the exciton dipole has been established. While the approximate model of Eq. (1) has already been successfully employed to comprehensively describe ultrafast exciton dynamics in dielectrics [14,19,20], we note that the applicability of ePIX is not limited to this particular formalism. Due to its extreme flexibility and being based on phase reconstruction algorithms, it is known in literature how to further develop the code in order to take into account for the contribution of different initial states [33,34], including coherent and incoherent effects [35]. As an example, in Sec. 7. we show how to include the effect of multiple coherent excitonic transitions.

Starting from $\epsilon(\omega, \tau)$, the system reflectance or absorbance can be evaluated through the Fresnel equations. Following the choice made in the most recent experiments [14,20], we concentrate on transient reflectance, $R(\omega, \tau)$. In case of s-polarized light, this quantity can be written as:

$$R(\omega, \tau) = \left|\frac{n_0\cos\theta - \sqrt{\epsilon(\omega,\tau) - n_0^2\sin^2\theta}}{n_0\cos\theta + \sqrt{\epsilon(\omega,\tau) - n_0^2\sin^2\theta}}\right|^2, \tag{4}$$

Optics EXPRESS

where n_0 is the refractive index of the surrounding medium, typically vacuum for experiments in the XUV spectral region (i.e. $n_0 = 1$), and θ is the angle of incidence, measured with respect to the surface sample normal.

Figure 1(a) shows a transient reflectance trace calculated with this model for an ideal system similar to what reported in Ref. [14]: at an angle of incidence $\theta = 73.5°$ and assuming physically-meaningful values for the parameters involved [19,36] as listed in Table 1. For relatively large delays, the trace shows a peak around the excitonic transition, $\omega = \omega_e$, corresponding to the quasi-particle contribution to the total reflectivity. Around the pump-probe temporal overlap (about 0 fs), we observe two major effects: (*i*) a blueshift of the excitonic peak, clear signature of the optical Stark effect and a non-zero α; (*ii*) the formation of additional structures about 3 eV above/below the excitonic peak, originating from the IR-field dressing of the excitonic resonance. Moreover, because of a finite γ, the reflectivity is modulated at twice the IR frequency.

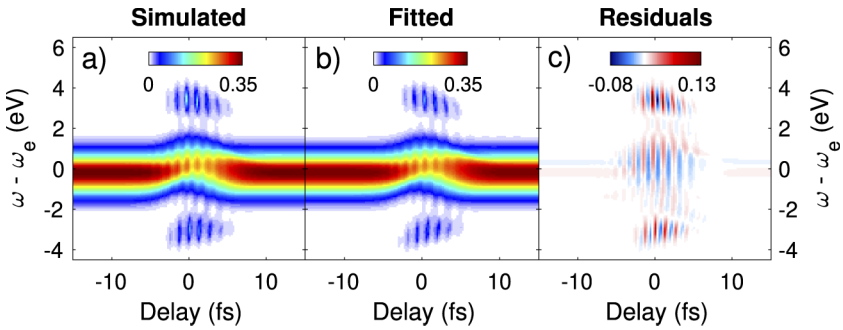

Fig. 1. (a) Simulated transient reflectance, $R(\omega, \tau)$, for an incidence angle of $\theta = 73.5°$, obtained by assuming an exciton Auger decay lifetime $T_e = 4$ fs, a phonon coupling and frequency $M_0 = 0.3$ PHz and $\omega_0 = 0.15$ rad PHz, respectively. The exciton frequency is $\omega_e = 84$ rad PHz. The IR pulse has a peak intensity of 0.78 V/Å and couples with the system through a complex polarizability of $(2 - i2.5)$ rad PHz Å^2 V^{-2}. The dipole amplitude is $k = 30$ PHz. The wavelength of the IR field is set to 800 nm, the full-width-half-maximum duration to 8 fs, the carrier-envelope phase (CEP) to $0.4\,\pi$ and its chirp rate to 0.05 fs^{-2}. (b) Result of a 2D least-square non-linear fitting procedure. (c) Residuals, defined as the difference between the fitted and simulated traces. The RMS of the fitted trace is $5.8 \cdot 10^{-3}$($RMS = \sqrt{\frac{\sum R_{fit} - R_{sim}}{M}}$, where R_{sim} and R_{fit} are the simulated and fitted traces, and M is the total number of data points).

Table 1. Simulated and retrieved values of the excitonic dipole $O(t)$ at the different stages during the ePIX algorithm. The indicated errors are the standard deviations arising from the results of four different reconstructions.

Parameter	Sim.	Fit	PIE I	ePIE	PIE II
α (rad PHz Å^2 V^{-2})	−5	-4.6 ± 0.013	-5.8 ± 2.7	-5.3 ± 0.75	-5.02 ± 0.038
γ (rad PHz Å^2 V^{-2})	2	1.5 ± 0.0088	1.0 ± 0.69	1.9 ± 0.36	2.01 ± 0.022
T_e (fs)	4	6 ± 0.092	3.8 ± 1	4.3 ± 0.55	3.99 ± 0.076
ω_e (rad PHz)	84	84 ± 0.00072	84.088 ± 0.1	83.96 ± 0.21	84.00 ± 0.0083
M_0 (PHz)	0.3	0.34 ± 0.0053	0.25 ± 0.058	0.32 ± 0.054	0.30 ± 0.0014
ω_0 (rad PHz)	0.15	0.11 ± 0.004	0.13 ± 0.036	0.16 ± 0.081	0.15 ± 0.0057
k (PHz)	30	27.2 ± 0.077	28.7 ± 3.1	28.8 ± 1.7	30.04 ± 0.23

Calculating $R(\omega, \tau)$ from the real-time dipole is generally an easy task, but the reverse problem is not trivial and extracting the real-time evolution of the excited state from a transient reflectance

Optics EXPRESS

measurement can be an hard task. A simple approach is to assume a parametric functional behaviour of the dipole moment and apply a non-linear fitting procedure to recover all the unknowns. This fitting approach is in general suitable for relatively simple dynamics; however, its application to retrieve the complex exciton behaviour may fail, without an *a priori* knowledge of some of the physical parameters which describe the system, in particular when the investigated dynamics evolve on time scales close to the time duration of the pump pulse. Without knowing any of the system characteristics, the fitting free parameters are: the exciton parameters T_e, ω_e, M_0, ω_0, k, and the IR pulse duration, phase, and chirp. When such a high number of unknown parameters is employed, we found the 2D fitting procedure to be at times inaccurate. This is mainly because similar reflectivity traces can be generated within a range of physical parameters, causing the fitting procedure to converge to different solutions depending on the initial guess. Indeed, while there is good qualitative agreement between the traces in Figs. 1, the retrieved parameters significantly differ from the ones used in the simulations (compare the second and third column in Table 1). In particular, the errors in the reconstruction of the Auger lifetime and the phonon parameters seem to compensate, thereby hindering a reliable access to the information underlying the transient reflectivity trace. Therefore, using a simple fitting procedure to interpret attosecond transient reflectivity traces without additional information can be misleading. In particular, depending on the dipole initial guess, the nonlinear fit can either converge to the right solution or to a wrong solution with comparable accuracy. If the initial dipole parameters are taken from random noise (as it will be done later with ePIX) the 2D fit does not converge. We stress that our intention is not to claim that a 2D fitting procedure is in general not accurate. If the initial parameters are not too far from the right solution, the fitting procedure delivers the correct answer. As we will discuss later, the new method we propose exhibits a superior robustness with respect to the initial parameters, allowing for the complete assessment of the core-exciton dynamics, regardless of its shape and complexity.

3. ePIX algorithm

In their standard implementation, ptychographic algorithms are based on the inversion of an internal product of the following form:

$$S(\omega,\tau) = \left| \int_{-\infty}^{+\infty} O(t)\, P(t,\tau)\, e^{i\omega t}\, dt \right|^2 \tag{5}$$

$$= \left| \mathcal{F}\left\{ O(t) \cdot P(t,\tau) \right\} \right|^2, \tag{6}$$

where $O(t)$ is the object to be reconstructed, $P(t)$ is called probe and $\mathcal{F}$ indicates the Fourier transform. When $P(t)$ is known, PIE [37] can be used to reconstruct the object $O(t)$. Instead, if both $P(t)$ and $O(t)$ are unknown, the ePIE algorithm is applied to retrieve both functions [38–40]. In case of transient absorption or reflectivity spectroscopy, the experimental traces cannot be written in the simple form of Eq. (5), preventing the direct application of ptychographic techniques. Nevertheless, if we define the object to be the excitonic dipole

$$O(t) = k\, H(t)\, e^{-\frac{t}{T_e}} e^{-i\omega_e t} e^{\Phi(t)}, \tag{7}$$

and the probe to equal the exponential describing the IR interaction

$$P(t,\tau) = e^{-\left(\gamma + i\frac{\alpha}{2}\right)\int_0^t E^2(t'-\tau)\, dt'}, \tag{8}$$

then Eq. (1) can be rewritten as:

$$\epsilon(\omega,\tau) = \epsilon_0 + \mathcal{F}\left\{ O(t) \cdot P(t,\tau) \right\} = \epsilon_0 + \widetilde{G}(\omega,\tau), \tag{9}$$

where the quantity $\widetilde{G}$ is the Fourier transform of $G(t,\tau) = O(t) \cdot P(t,\tau)$. Equation (9) underlines the parallelism between Eq. (5) and the excitonic contribution to the total permittivity. While

Optics EXPRESS

this suggests the possibility to use ptychographic techniques to reconstruct the exciton dynamics, their applicability is not straightforward. Since $\epsilon(\omega,\tau)$ is subsequently related to the transient reflectivity by Eq. (4), in this case $O(t)$ and $P(t,\tau)$ are not related to the experimentally-measured quantity through a simple inner product as in Eq. (5), but rather by:

$$S(\omega,\tau)=\left|\frac{n_0\cos\theta-\sqrt{\epsilon_0+\mathcal{F}\left\{O(t)\cdot P(t,\tau)\right\}-n_0^2\sin^2\theta}}{n_0\cos\theta+\sqrt{\epsilon_0+\mathcal{F}\left\{O(t)\cdot P(t,\tau)\right\}-n_0^2\sin^2\theta}}\right|^2. \tag{10}$$

In principle, one might think that this additional mathematical complexity could hinder convergence, but this is not the case. Since the electric dipole moment $O(t)$ respects the causality principle, leading to a Kramers-Krönig-consistent permittivity, the reconstruction problem is well-posed [41]. Nevertheless, to assure robust convergence, within the ePIX algorithm PIE and ePIE need to be applied in a non-conventional manner. The algorithm block diagram is shown in Fig. 2. At first, the IR pulse is assumed to be known and the PIE algorithm is run to retrieve the object and the exciton complex polarizability $\alpha/2-i\gamma$. This assumption does not constitute a severe limitation as an educated guess for the IR pulse is typically available in attosecond experiments, *e.g.* obtained as a side-product of the attosecond pulse characterization through attosecond streaking. In certain cases the IR pulse is measured simultaneously with the transient reflection/absorption experiment, assuring higher temporal resolution [42]. As an alternative, the initial guess for the IR field can be derived from an independent optical measurement using, for example, the Frequency-Resolved Optical Gating (FROG) [43] or the Spectral Phase Interferometry for Direct Electric-field Reconstruction (SPIDER) [44] techniques. If the IR initial guess is accurate, this first PIE reconstruction is sufficient; if not, the excitonic polarizability is fixed to the current value and an ePIE reconstruction is performed to update both the object and the IR electric field. Following the iterative approach depicted in Fig. 2, the result achieved by the ePIE stage can then be fed back to the PIE stage, if necessary.

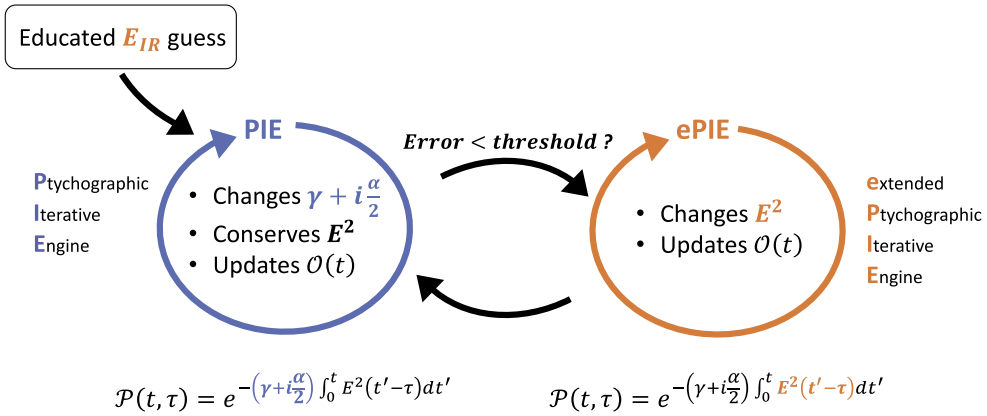

Fig. 2. Scheme of the ePIX reconstruction algorithm. The first stage (PIE) modifies the complex polarizability. After a certain reconstruction error has been achieved, the second stage (ePIE) is applied to correct also the IR field prediction. The result can then be fed back to the PIE stage as described in the main text, in case convergence requires further iterations. We found that a progression of three to five iterations is typically enough to reach convergence.

To assure efficient convergence of the first reconstruction stage (PIE) we introduced two constraints on $P(t,\tau)$, which enforce the correct functional shape on the probe. This approach is analogous to the pure-phase constraint applied in the context of attosecond pulse ptychographic

Optics EXPRESS

reconstruction [26]. In particular, at each iteration we impose for the module ($|\cdot|$) and phase ($\angle\{\cdot\}$) of $P(t)$

$$\begin{cases} |P(t)| - e^{-\gamma I} = 0 \\ 2\angle\{P(t)\} + \alpha I = 0, \end{cases} \tag{11}$$

where

$$I = \int_0^t E^2(t')\,dt', \tag{12}$$

is the integral of the modulus squared of the IR field. These constraints are applied in the least-norm sense: at each iteration, the new values of α and γ are evaluated by minimizing the norm of the left-hand side of Eqs. (11). The updated value of the probe is thus given by:

$$P(t,\tau) = e^{-\left(\gamma' + i\frac{\alpha'}{2}\right)\int_0^t E^2(t'-\tau)\,dt'}. \tag{13}$$

In this way it is possible to partially update the probe (polarizability) keeping the IR pulse unchanged. In this regard, our PIE stage differs from standard PIE applications, where the complete probe $P(t, \tau = 0)$ does not change through the reconstruction.

Due to the complexity of the problem under examination, also the application of the second ePIE stage is not straightforward. The peculiar functional relation between reflectivity and permittivity, together with the presence of a complex polarizability which multiplies the electric field integral, can, in certain cases, prevent a fast convergence. To overcome this limitation, we follow an approach similar to that implemented by Keathley et al. [45] and assume the IR vector potential, $A(t)$, to have a known analytical form (i.e. Gaussian envelope and quadratic chirp). In this way, at each iteration the code needs to update only a reduced set of parameters three in our case), which fully describe $A(t)$, increasing the convergence speed. In particular, we suppose the IR vector to be adequately described by the following form:

$$A(t) = A_0 e^{-\frac{t^2}{T_L^2}4\ln 2}\cos\left(\omega_L t + \frac{\beta_L}{2}t^2 + \phi_L\right), \tag{14}$$

where A_0 is the amplitude, T_L is the amplitude FWHM, ω_L is the IR frequency, β_L is the chirp rate and ϕ_L is the carrier-envelope phase (CEP). The IR field $E(t)$ is then evaluated as $E(t) = -\partial A(t)/\partial t$. Since the interaction with the IR field is proportional to its square value, the CEP is only defined modulus π. All the The CEP values reported in this work are thus to be intended in this way.

4. Results

In order to test the validity of ePIX, we applied our algorithm to the simulated trace of Fig. 1(a). Besides reproducing the behaviour of a physical problem, it represents an ideal test-case as all the physical parameters which can alter the transient optical response of the system are present. It is worth mentioning that the approach reported here is not limited to this specific physical case. We test ePIX against different optical field and exciton parameters and found that only few iterations of the PIE-ePIE stages (typically less than two) are required to converge with comparable results in all cases. We note that it is beneficial to end the ePIX procedure with a PIE stage, as this allows for a final refinement of the probe function, assuring better reconstruction than the 2D fitting procedure. The results we present are obtained by averaging a set of four different reconstructions of the same reflectivity trace, starting by different initial guesses of the involved quantities. Performing several runs of the algorithm with different initial parameters is common procedure used to estimate the accuracy of the reconstruction and not to improve the reconstruction results. In the present case, we found that a set of 4 different initial parameters

Optics EXPRESS

was enough to obtain a robust estimate of standard deviation of the retrieved parameters. The output of the single reconstruction, which consists in approximately 1000 loops of the iterative algorithm and can require up to 30 minutes, statistically lies within the intervals reported in Table 1.

4.1. First stage: PIE

The first step of the reconstruction consists in the application of the PIE algorithm described above. Assuming no *a priori* knowledge on the exciton physical parameters, the initial guess of $O(t)$ is set to white noise while α and γ are set to reasonable values, but different from the exact solutions, as summarized in Table 2. The input reflectivity trace is simulated with a Gaussian IR pulse having a FWHM time duration of 8 fs, central wavelength of 800 nm, a carrier-envelope phase (CEP) of $0.4\,\pi$ and a chirp rate of $0.05\ \mathrm{fs}^{-2}$ (black curve in Fig. 3). Assuming a non-perfect knowledge of the IR, we perform four different reconstructions where the initial guesses are Gaussian pulses with a duration of either 5.6 or 10.3 fs, a CEP of 2.0 or 0.5 rad and a chirp rate of 0 or $0.1\ \mathrm{fs}^{-2}$ (two examples are reported in Fig. 3, dotted curves).

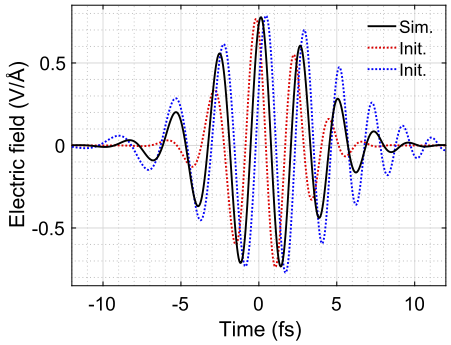

Fig. 3. Simulated IR field (black curve) and two examples of IR initial guesses (dotted red and blue curves). For the simulated field, the wavelength is set to 800 nm, the amplitude FWHM duration to 8 fs, the carrier-envelope phase (CEP) to 1.26 rad and its chirp rate to $0.05\ \mathrm{fs}^{-2}$. The initial guesses used in the reconstructions differ from the simulated field in duration, phase and chirp.

Table 2. Initial guesses for the different parameters which characterize the probe and object. The initial guess for the dipole moment $O(t)$ is random noise. For the other parameters, two possible initial guesses are given: the four reconstructions explore different combinations of these initial guess values.

Parameter	Simulated	Initial guess
$O(t)$	Eq. (7)	Random noise
α (rad PHz Å^2 V^{-2})	−5	−8 or −2
γ (rad PHz Å^2 V^{-2})	2	0.5
FWHM (fs)	8	5.6 or 10.3
CEP (rad)	1.26	2 or 0.5
β_L (fs^{-2})	0.05	0 or 0.1

The scope of this approach is to test the accuracy of the reconstruction with a non-perfect knowledge of the IR pulse and to stress-test the reconstruction of the dipole moment parameters.

Figure 4 shows the result of the first PIE stage, averaging over the four reconstructions performed. The reconstructed trace of Fig. 4(b) already qualitatively agrees with the simulated

Optics EXPRESS

input (Fig. 4(a)). By assuming a non-perfect IR pulse (Fig. 3), the quantities which strongly depend on the exact IR field are not properly reconstructed (e.g. the oscillation phase of the sideband signals almost 3 eV away from the main band). Nevertheless, the reconstructed excitonic dipole amplitude and phase (red dashed curve in Fig. 4(c)), largely agree with the simulation input (black-solid curve), within the reconstruction uncertainty (represented by the red shaded area which extends over two standard deviations). The overall agreement is further confirmed by the retrieved exciton physical parameters (see Section 5) and demonstrates that qualitative information can be extracted from the transient reflectance trace with no prior information on the exciton dipole moment and without a perfect knowledge of the IR pulse. This result motivates the choice for a subsequent ePIE application to polish the reconstruction of both object and probe.

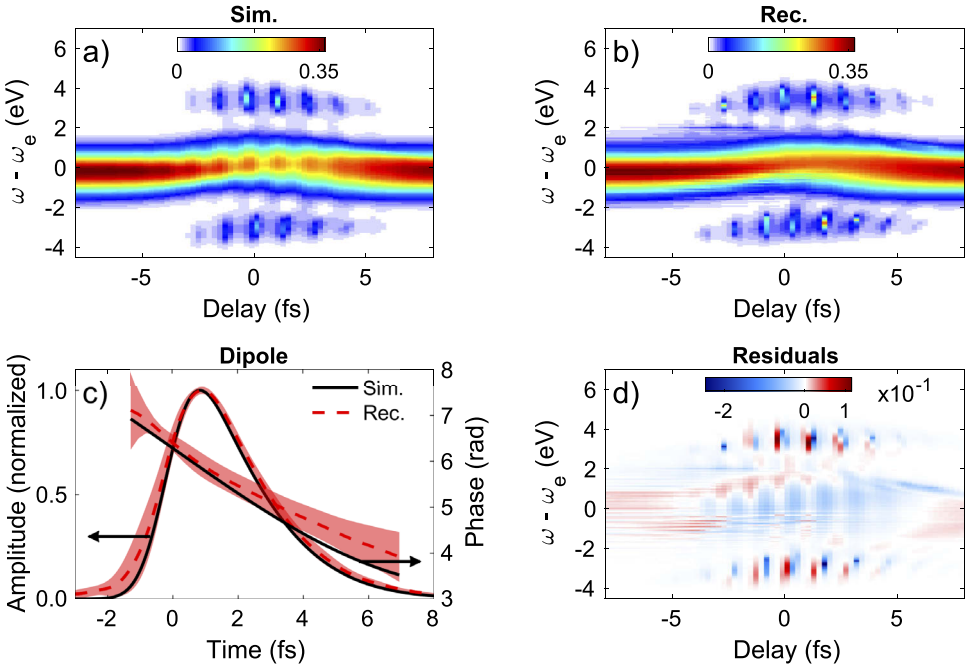

Fig. 4. Simulated, (a), and reconstructed, (b), transient reflectance trace, after the first PIE stage of the ePIX algorithm. (c) Input (solid black) and reconstructed (red dashed) excitonic dipole $O(t)$ amplitude and phase. (d) Difference between the reconstructed and simulated traces. The reconstructed dipole shows already a good degree of qualitative agreement after this first stage. The RMS of the reconstructed trace is $8.9 \cdot 10^{-3}$.

4.2. *Second stage: ePIE*

If the IR pulse is not known with enough accuracy, as for the present case, the ePIE stage might be needed to refine the results. The output of the previous step becomes the new initial guess for this stage, where the algorithm updates object and IR field as described in Section 3. The results obtained after approximately 1000 iterations of the ePIE step are displayed in Fig. 5. As this stage updates the IR field, the smaller details, like the phase of the sideband oscillations, are perfectly recovered and the agreement between the simulated (Fig. 4(a)) and the reconstructed (Fig. 5(a)) reflectivity traces is improved by one order of magnitude (compare the residuals in Fig. 4(d) with the ones of Fig. 5(b)). Moreover, the better accuracy in the reconstruction of the reflectivity trace is translated to a more precise retrieval of both the excitonic dipole and IR electric field time evolution (Figs. 5(c) and 5(d), respectively). Table 3 summarizes the values of the IR field

Optics EXPRESS

parameters retrieved by the last ePIE stage employed in ePIX. The good agreement between reconstructed and simulated parameters confirms the ability of the ePIE stage in recovering the correct IR field.

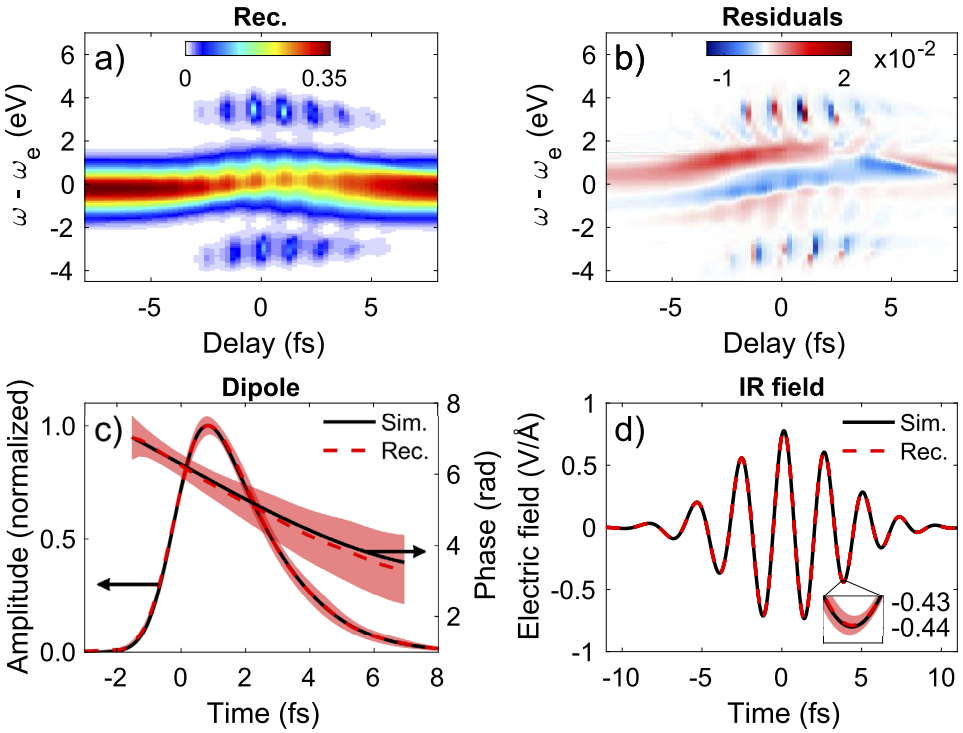

Fig. 5. Reconstructed reflectivity trace (a) and map of the residuals (b), as a result of the last ePIE stage in the ePIX algorithm. Panels (c) and (d) show the reconstructed dipole moment and IR field, respectively: in both panels the exact solution is presented with solid black curves while the reconstruction results are with dashed red curves. The shaded red areas represent the standard deviation calculated over the four different reconstructions performed. The recovery of the IR field resulting from the application of ePIE leads to a more accurate reconstruction of the reflectivity trace, as can be seen by comparing the residuals with the ones in Fig. 4(d). The RMS of the reconstructed trace is $1.1 \cdot 10^{-3}$.

Table 3. Simulated and retrieved values of the IR field parameters after the last ePIE stage in the ePIX algorithm. The indicated errors are the standard deviations, arising from the results of four different reconstructions.

Parameter	Simulated	ePIE retrieval
FWHM (fs)	8	7.99 ± 0.046
CEP (rad)	1.26	1.25 ± 0.013
β_L (fs^{-2})	0.05	0.051 ± 0.0035

4.3. *Final PIE polishing*

Despite the outstanding results obtained after the ePIE stage discussed above, we found beneficial to close the ePIX algorithm with the application of a PIE stage in order to further refine the excitonic dipole in view of the more accurate IR guess obtained. Following the ePIX iterative

Optics EXPRESS

approach, this final step takes as input parameters the output of the previous step. The IR electric field is fixed while the excitonic dipole and polarizability are updated. After about 1000 iterations of the PIE code, the maximum discrepancy of the reconstructed dipole is 0.42% of the peak amplitude and 14 mrad for the phase (see Fig. 6(a)), showing the high accuracy of our algorithm.

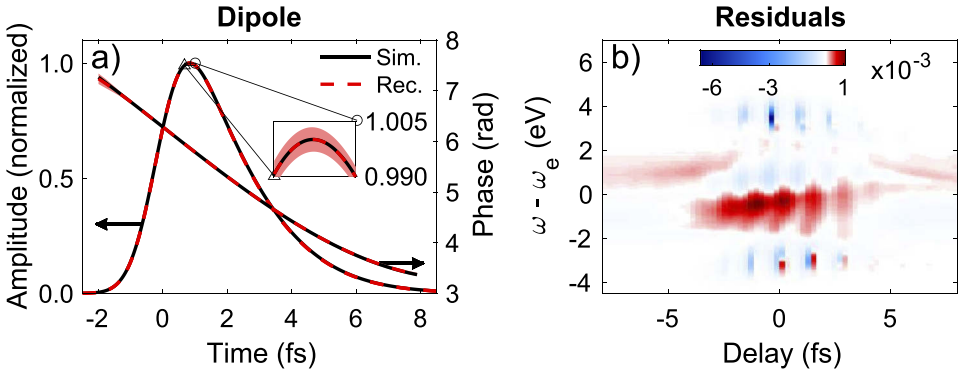

Fig. 6. (a) Exact (solid black) and final ePIX reconstructed (dashed red) dipole moment $O(t)$ in amplitude and phase. (b) Associated map of the residuals. Both amplitude and phase are correctly recovered with very small uncertainty. As the last stage in the ePIX algorithm does not update the IR field, the final IR reconstruction is the same as Fig. 5(d). The RMS of the reconstructed trace is $1.4 \cdot 10^{-4}$.

5. Discussion

In this Section, we compare the exciton physical parameters obtained at each ePIX stage. To this end, for each of the three steps described in Section 4, we fit the resulting exciton dipole with the 1D fitting curve given by Eq. (7). The retrieved parameters are summarized in Table 1, where the reported errors are the standard deviations arising from the results of four different reconstructions. Notice that the right order of magnitude for the parameters is retrieved already at the first reconstruction step (PIE I, third column in Table 1), even if the IR field is not accurately known. Indeed, the estimated values agree with the exact theoretical quantities within less than 20% relative error (except for γ, which clearly requires further reconstruction steps to be more accurately recovered). The subsequent ePIE step corrects the IR estimation, considerably refining the exciton parameters (fourth column in Table 1) which now agree with the exact values within a 10% relative error. The last step (PIE II, fifth column in Table 1) reduces the reconstruction uncertainty, improving the overall accuracy. We found the final output parameters to agree with the theoretical values with high degree of accuracy. To better display the effect of the subsequent reconstruction steps, in Fig. 7 we show the evolution of the Auger lifetime (Fig. 7(a)) and phonon coupling (Fig. 7(b)) through ePIX. While the second ePIE step changes significantly the parameter estimation, the third step does not correct the mean value significantly, but rather increases the reconstruction accuracy as marked by the smaller error bars. These results not only prove the transient reflectance trace to be sensitive to the exciton properties, but also that the ptychographic-based algorithm we developed is well-founded, demonstrating to be a valuable tool for the investigation of exciton dynamics in transient reflectance measurements. To further check this, we applied the ePIX method to various transient reflectance traces generated with different physical parameters. We found our approach to converge in all cases with the same accuracy discussed here. If some of the physical parameters are known *a priori*, both ePIX convergence and accuracy are boosted. What we discussed in this work is a "worst-case scenario", where no physical parameter is known and an accurate IR time characterization is not available.

Optics EXPRESS

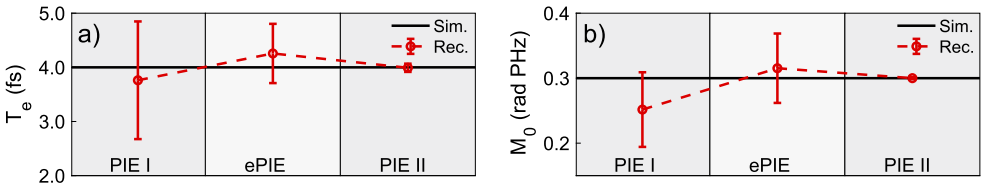

Fig. 7. Reconstructed Auger lifetime (a) and phonon coupling (b) as a function of the reconstruction stage in ePIX. Note that the average value of each parameter approaches the simulated value, and the error bar narrows. A similar behaviour is observed for all other parameters.

For the sake of simplicity, all the calculations and reconstructions reported here include only the exciton ground state contribution to the transient reflectivity trace. Nevertheless, in a real experiment, the transient reflectivity trace $R(\omega, \tau)$ is more likely to contain features related to several excitonic transitions, including dark states which become optically active under the effect of the driving IR field. While this hinders the direct application of the model described in this Section to experimental traces, the ePIX approach remains valid as it does not assume a particular functional shape for the object $O(t)$ (excitonic dipole) and can therefore be extended to account for different excitonic transitions. Of course, in such a case, the model used to perform the 1D fit and extract the physical parameters of interest needs to be changed accordingly. It is worth noticing that, in case of congested spectra, the ePIX accuracy might be reduced because of the large number of free parameters to be reconstructed. Nevertheless, we expect our approach to perform better than a 2D fit of the transient reflectance trace. Indeed, with the ePIX method we can unambiguously determine all the parameters that govern the ultrafast dynamics of a core exciton and its interaction with the crystal, such as its Auger lifetime or the coupling with the phonons. The understanding of such properties is crucial for shedding new light on the behaviour of solid-state materials and assessing their features with unprecedented accuracy. Therefore, our reconstruction algorithm, together with the experimental methods of the attosecond science, may serve the purpose of widening the knowledge about light-matter interaction, paving the way for a full comprehension and control of its optoelectronic properties, up to the petahertz regime.

6. Effect of noise

To prove the applicability of ePIX to imperfect experimental traces, we studied its robustness with respect to white noise. In particular, we added to the simulation of Fig. 4 a white noise with standard deviation equal to 10% of the maximum value of the reflectivity. The noisy trace (Fig. 8(a)) is then fed to the ePIX algorithm whose reconstruction result is reported in Fig. 8. We note that this represents an extreme condition. In a real experiment the noise level could be strongly reduced with opportune filtering [46], prior reconstruction.

Due to the high noise level, the smaller features in the trace of Fig. 8(a) are strongly affected, preventing a clear observation of the oscillations in the sidebands. Nevertheless, the agreement between the simulated and reconstructed dipole moment (Fig. 8(b)) is satisfactory, both in terms of amplitude and phase. The main physical parameters extracted with the 1D fitting procedure discussed in the previous sections are reported in Table 4, both for the dipole moment and for the IR field. Despite the high noise level, the parameters are largely recovered by the ePIX approach, with the only exceptions of the IR chirp rate and imaginary part γ of the complex polarizability. These parameters are the most sensible to the oscillating features of the transient reflectivity trace, so that the presence of a significant amount of noise hinders their reconstruction. The overall robustness of ePIX to extreme noise is in line to what found for standard ptychographic algorithms, upon which it is based [26,47,48]. If the signal-to-noise ratio is kept above 17, ePIX

Optics EXPRESS

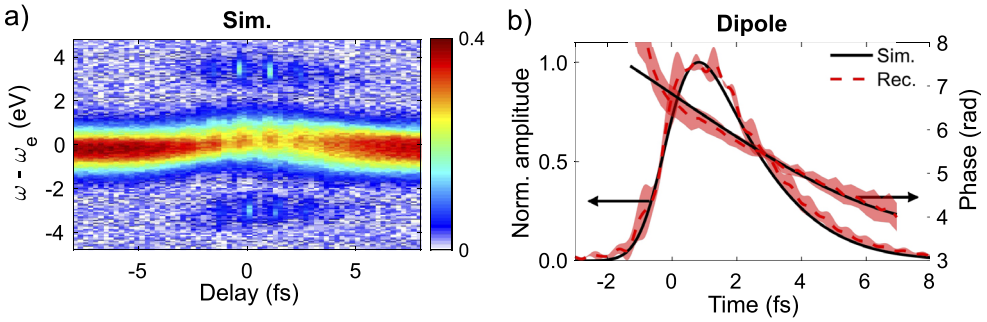

Fig. 8. Simulated transient reflectivity trace (a), with the addition of 10% rms white noise. (b) Input (solid black) and reconstructed (red dashed) excitonic dipole $O(t)$ amplitude and phase. The reconstructed dipole shows a good qualitative agreement, despite the high level of noise.

correctly converges to the exact solution, also for induced relative changes $\Delta R/R$ of the order of few percent.

Table 4. Simulated and ePIX retrieved physical parameters, in the presence of 10% rms white noise. The indicated errors are the standard deviations, arising from the results of three different reconstructions.

Parameter	Simulated	ePIE retrieval
α (rad PHz Å^2 V^{-2})	−5	-5.2 ± 1.7
γ (rad PHz Å^2 V^{-2})	2	0.6 ± 0.6
T_e (fs)	4	3.6 ± 1
ω_e (rad PHz)	84	84.07 ± 0.15
M_0 (PHz)	0.3	0.24 ± 0.023
ω_0 rad PHz)	0.15	0.09 ± 0.05
k (PHz)	30	30.5 ± 2
FWHM (fs)	8	7.8 ± 0.95
CEP (rad)	1.26	1.23 ± 0.42
β_L (fs^{-2})	0.05	0 ± 0.5

While one would be tempted to apply ePIX directly to $\Delta R/R$ to reduce the experimental noise, we note that the loss of information will prevent the code to converge unless the static reflectivity is directly given to the code, which is the same as having a certain a-priori knowledge of the physical system under investigation.

7. Multiple excitation

Real physical systems are often characterized by the presence of multiple excitonic transitions, which can be simultaneously probed by a short, broadband XUV pulse. If this is the case, the total material permittivity of Eq. (1) contains the coherent contribution of each final state. Here we prove that ePIX can be successfully applied also to this scenario by simulating and reconstructing the transient reflectivity associated to the first two excitonic states of MgO around the Mg $L_{2,3}$ edge [20].

As reported by R. Géneaux and coworkers, the excitonic dipole can be expressed as a sum of single-transition contributions. If we concentrate on the first two excitonic transitions, the total

Optics EXPRESS

permittivity can thus be written as:

$$\epsilon(\omega,\tau) = \epsilon_0 + \int_{-\infty}^{+\infty} \left[O_1(t)P_1(t,\tau) + O_2(t)P_2(t,\tau)\right] e^{i\omega t}\, dt, \tag{15}$$

where each excitonic dipole O_i has the form:

$$O_i(t) = k_i H(t)\, e^{-\frac{t}{T_e}} e^{-i\omega_{e,i}t} e^{\Phi_i(t)}, \tag{16}$$

and $\Phi_i(t)$ is the phonon contribution given by:

$$\Phi_i(t) = -\frac{M_{0,i}^2}{\omega_0^2}\left[(2N+1)(1-\cos\omega_0 t) - i(\omega_0 t - \sin\omega_0 t)\right]. \tag{17}$$

While the excitation energy, $\omega_{e,i}$, the amplitude, k_i, and phonon coupling, $M_{0,i}$, depend on the particular excitation ($i = 1, 2$), the Auger decay time, T_e, the phonon frequency, ω_0, and population, N, are the same for the first two excited states [20]. Since the initial thermal phonon population is low ($N \simeq 0.09$), we chose $N = 0$ in our simulations. For what concerning the coupling with the IR field, we consider the most general case where the probe P_i depends on the particular transition through the complex polarizability:

$$P_i(t,\tau) = e^{-i\left(\gamma_i + \frac{\alpha_i}{2}\right)\int_0^t E^2(t'-\tau)dt}. \tag{18}$$

Fig. 9(a) shows the simulated MgO reflectivity obtained by substituting the permittivity of Eq. (15) into Eq. (4) and using the physical parameters reported in Table 5. The IR pulse is assumed to be Gaussian, transform limited, with duration FWHM of 6 fs, central wavelength of 800 nm and peak intensity equal to 9×10^{12} W cm^{-2}.

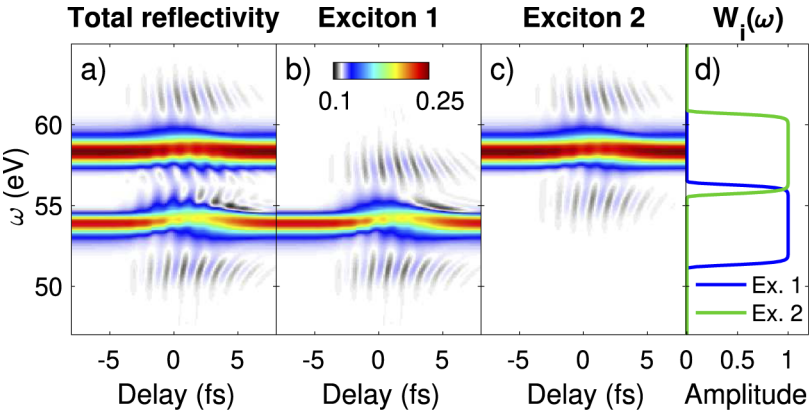

Fig. 9. (a) Simulated transient reflectivity trace for the first two core excitonic states around the Mg $L_{2,3}$ edge in MgO [20]. The trace is given by the coherent sum of two contributions, (b) and (c), arising from the two excitonic transitions. (d) Spectral weight functions, $W_i(\omega)$, used in Eq. (20) to build the update function used by the ePIX algorithm (see related discussion in the text).

Even if the initial transitions are more than 4 eV apart, the individual contributions (Figs. 9(b),(c)) partially overlap in energy and cannot be reconstructed simply by considering separate portions of the spectrum. In order to apply the ePIX algorithm and be able to disentangle the two contributions, we rewrote the total permittivity of Eq. (15) as:

$$\epsilon(\omega,\tau) = \epsilon_0 + \mathcal{F}\left\{O_1(t)\cdot P_1(t,\tau)\right\} + \mathcal{F}\left\{O_2(t)\cdot P_2(t,\tau)\right\}. \tag{19}$$

The ePIX code runs as for the case of a single excitation (see Appendix 8), with the subsequent application of the PIE and ePIE stages, simultaneously updating $O_1(t)$, $O_2(t)$, $P_1(t)$ and $P_2(t)$.

Optics EXPRESS

Table 5. Simulated and retrieved excitonic dipole and IR parameters, in the presence of multiple excitonic transitions. The indicated errors correspond to the standard deviations, arising from the results of four different reconstructions.

Parameter	Simulated	ePIE retrieval
α_1 (rad PHz Å^2 V^{-2})	−4	-4.04 ± 0.084
α_2 (rad PHz Å^2 V^{-2})	−2	-2.04 ± 0.12
γ_1 (rad PHz Å^2 V^{-2})	1	1.03 ± 0.073
γ_2 (rad PHz Å^2 V^{-2})	0.5	0.48 ± 0.041
T_e (fs)	138	10000 ± 5000
$\omega_{e,1}$ (rad PHz)	81.74	81.81 ± 0.031
$\omega_{e,2}$ (rad PHz)	88.42	88.43 ± 0.0086
$M_{0,1}$ (PHz)	0.40	0.39 ± 0.0074
$M_{0,2}$ (PHz)	0.56	0.54 ± 0.01
ω_0 rad PHz)	0.09	0.09 ± 0.044
k_1 (PHz)	15	14.66 ± 0.41
k_2 (PHz)	24	23.92 ± 0.34
FWHM (fs)	6	5.78 ± 0.30
CEP (rad)	0	-0.0039 ± 0.0095

The total product function $G^{'}(t,\tau)$ of Eq. (22), used by the code to update the objects and probes, is then given by:

$$G'(t,\tau) = G'_1(t,\tau) + G'_2(t,\tau), \tag{20}$$

with

$$G'_i(t,\tau) = \mathcal{F}^{-1}\left\{\widetilde{G}'(\omega,\tau)\, W_i(\omega)\right\} \quad (i = 1,2), \tag{21}$$

where $\widetilde{G}'$ is the Fourier transform of $G'(t,\tau)$ and $G'_i(t,\tau)$ is the temporal product between object and probe of a single transition, updated by an ePIX iteration as described in the Appendix. $W_i(\omega)$ is a spectral weight function: its exact shape of the weight function can be adjusted according to the specific experimental physical system under study. For the present case, we used a supergaussian bell centred at the excitonic transition, wide enough to include the exciton spectrum (Fig. 9(d)).

Figure 10 reports the reconstruction results. The reconstructed transient reflectivity trace (Fig. 10(b)) is in good agreement with the simulated one (Fig. 10(a)) and the same holds for the total excitonic dipole (Fig. 10(c)), given by the coherent sum of the two transitions, and the IR pulse (Fig. 10(d)). Working directly on the single-transition dipole moments, the total dipole of Fig. 10(c) can be directly decomposed in the two contributions $O_1(t)$ and $O_2(t)$ (Figs. 10(e) and 10(f)) from which the associated physical parameters can be extracted as discussed in Sec. 4. The results are listed in the second column of Table 5. All the parameters are properly reconstructed except the Auger lifetime T_e. This is not a limitation of the ePIX approach, but rather peculiar of the case under study. As reported in Ref. [20], the population decay rate due to the phonon coupling is much faster than the Auger lifetime of the Mg 2p hole involved (few fs vs. hundreds of fs). The total dipole decay is hence dominated by the phononic term, and the simulated dipole moments and the transient reflectivity trace are largely insensitive to the exact value of T_e. We stress the fact that the Auger lifetime T_e is not adequately recovered not because of an intrinsic limit of the ePIX algorithm, but rather because of the insensitivity of the exciton dipole $O(t)$ time-evolution with respect to T_e. Indeed, the dipole moments are correctly retrieved, as shown in Fig. 10, even if T_e is not. In general, the excitonic dipole will be sensitive both to the Auger

Optics EXPRESS

and phonon coupling processes only when the two induce comparable decays. In general, if the experimental trace is not sensitive to a specific parameter of the model, we found ePIX to converge to an inaccurate result. Those bad parameters can thus be identified by running ePIX more than once and by evaluating the associated standard deviation as done in the present case.

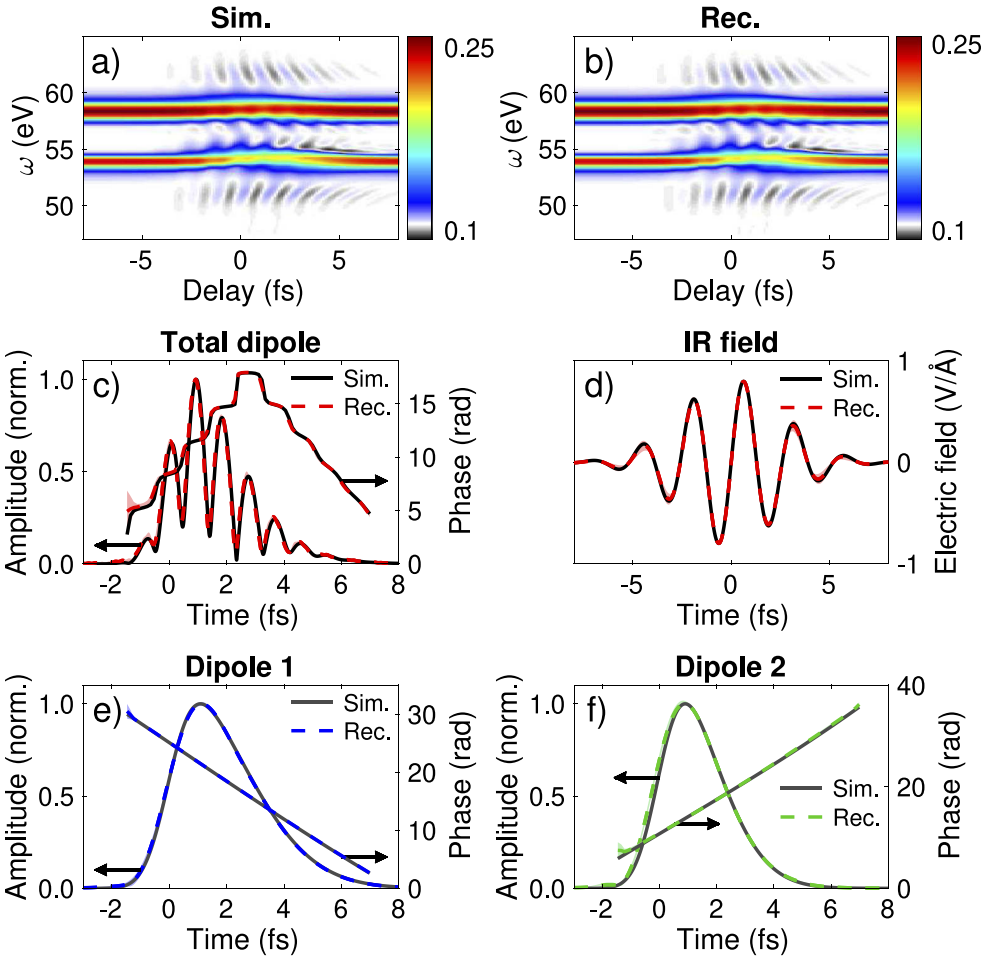

Fig. 10. Simulated (a) and reconstructed (b) transient reflectivity trace, for the first two core excitonic states around the Mg $L_{2,3}$ edge in MgO [20]. (c) Simulated (solid black) and reconstructed (red dashed) total excitonic dipole ($O_1(t) + O_2(t)$) amplitude and phase. (d) Simulated (solid black) and reconstructed (red dashed) IR pulse. (e), (f) Individual dipole moments, $O_1(t)$ and $O_2(t)$, describing the two excitonic transitions. The simulation results are reported in solid black while the direct ePIX reconstructions are represented by the dashed blue and green curves for the excitonic ground state and its first excited state, respectively.

Without pretending to comprehensively describe all possible physical scenarios (certainly behind the scope of this work), the results reported in this Section already demonstrate the applicability of ePIX to more realistic systems where the total response is characterized by the coherent sum of multiple excitations.

Optics EXPRESS

8. Conclusions

In this work, we presented a novel approach, named ePIX, to recover the ultrafast core-exciton dynamics from transient reflectivity measurements. This method is based on a reformulation of the PIE and ePIE algorithms in an iterative approach. By applying ePIX to a simulated transient reflectivity trace, computed in conditions similar to what reported in Ref. [14], we prove that the method is capable of accurately reconstructing the exciton dynamics even with no *a priori* knowledge of any of the physical parameters which describe the system and with little knowledge of the IR driving electric field, given that the experimental trace is actually sensitive to the sought parameter. The results are tested against white noise and compared with a more common 2D fitting procedure, showing superior degree of accuracy and sensitivity against the complexity of the physical phenomena under examination. Finally, as the approach we proposed is based on an atomic-like description, ePIX can be applied beyond the field of solid-state physics, becoming a valuable tool for studying the ultrafast dynamics in different physical scenarios.

Appendix: The ePIX algorithm

The ePIX algorithm is based on the extended ptychographic iterative engine (ePIE), although with some major differences. The schematic of Fig. 11 represents a single iteration of the algorithm, which runs over each delay of the experimental trace, updating each time both the object, $O(t)$, and the probe, $P(t)$. The procedure starts with an initial guess, which is typically random noise for the object and a Gaussian shape for the IR pulse. At the actual delay τ under consideration, first the object is delayed by $-\tau$ in order to evaluate the product:

$$G(t,\tau) = O(t+\tau)\,P(t+\tau,\tau) = O(t+\tau)e^{-(\gamma+i\frac{\alpha}{2})\int_{-\tau}^{t} dt' E^2(t')}. \tag{22}$$

In this way the lower extreme of the integral in P follows the arrival time of the excitation described in O.

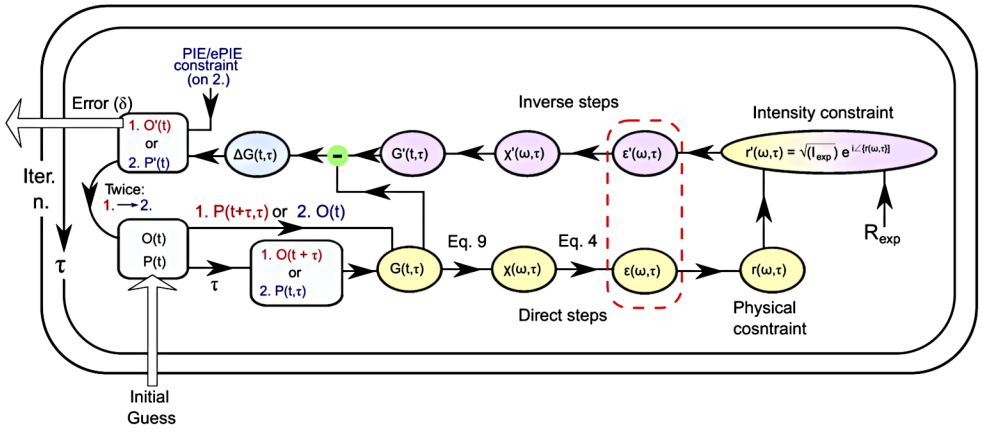

Fig. 11. Schematic representation of the ePIX iterative algorithm. For each delay, the reported steps are repeated twice, updating in sequence object $O(t)$ (steps indicated with the number 1), and then the probe $P(t,\tau=0) \equiv P(t)$ (steps indicated with the number 2). When the probe is updated, PIE or ePIE constrains are applied before moving to the next delay point, depending on which stage the ePIX algorithm is currently running. Once the probe is updated, the cycle is repeated until all the delay points are covered, completing a full iteration of the algorithm.

Due to the definitions of O and P within ePIX, $G(t,\tau)$ represents the temporal evolution of the exciton dipole, perturbed by the IR field (integrand of Eq. (1)). From this, assuming a value for

Optics EXPRESS

the background permittivity ϵ_0, we can compute the dynamical electrical permittivity $\epsilon(\omega, \tau)$ through Eq. (9). Starting from this quantity it is possible to compute the associated reflection or absorption, to be compared with the experimental results. In the present case, investigating the reflectivity of the material to s-polarized light at a given incidence angle θ, ePIX computes the complex reflection coefficient through the Fresnel equation:

$$r(\omega, \tau) = \frac{n_0 \cos\theta - \sqrt{\epsilon(\omega, \tau) - n_0^2 \sin^2\theta}}{n_0 \cos\theta + \sqrt{\epsilon(\omega, \tau) - n_0^2 \sin^2\theta}}. \tag{23}$$

The code can now apply the intensity constraint directly to this quantity, keeping the phase of the calculated $r(\omega, \tau)$, but substituting its amplitude with the square root of the measured energy dependent reflectance, $R_{exp}(\omega, \tau)$ at the specific delay under consideration. These last steps constitute the major difference between ePIX and standard ptychographic iterative algorithms where the intensity constraint is directly applied to the Fourier transform of $G(t, \tau)$. In the present case, the intensity constraint must be applied on the Fresnel coefficient $r(\omega, \tau)$, which is not a simple inner product between the object and the probe (see Eq. (10)), as for the case of the PIE and ePIE algorithms. Once the amplitude of the Fresnel coefficient has been updated, the code performs the inverse calculations to retrieve the updated function $G'(t, \tau)$ by employing the equation

$$G'(\omega, \tau) = \left\{\frac{1 - r'(\omega, \tau)}{1 + r'(\omega, \tau)}\right\}^2 n_0^2 \cos\theta^2 + n_0^2 \sin\theta^2 - \epsilon_0 \tag{24}$$

and computes the difference $\Delta G(t, \tau) = G'(t, \tau) - G(t, \tau)$, which is used to update the object function. Before moving to the next delay step, as done in PIE or ePIE, the code repeats the cycle but updating the probe instead of the object. Starting from the initial guess of $P(t, 0)$, the code calculates $P(t, \tau)$ by delaying the electric field $E(t)$ included in the definition of P. Then, the quantity $G(t, \tau) = P(t, \tau)\, O(t)$ is evaluated. The algorithm steps proceed identical in order to retrieve a new difference $\Delta G(t, \tau)$, used this time to update the probe. In this case, depending on the current ePIX stage, the algorithm set either the PIE or ePIE constraint to the updated probe $P'(t, 0)$ (Fig. 2). During the PIE stage, the IR electric field is kept constant and the code only updates the complex polarizability. During the ePIE stage, instead, the complex polarizability is kept constant and the IR field is updated. In this latter case, to help convergence, the electric field is fitted to a known analytical shape, composed by an envelope function (e.g. a Gaussian bell) multiplied by a sinusoidal with a time dependent frequency (to account for a possible chirp).

At this step the code moves to the next delay point, using as initial guess the updated object and probe functions, $O'(t)$ and $P'(t)$, obtained at the previous delay. Once all the delay points of the input trace have been evaluated the code has performed one full iteration. The current values of O and P are used to compute the complex reflection coefficient (Eq. (10)), and the reconstruction error can be evaluated as:

$$\delta = \frac{\sum_{n_\omega=1}^{N_\omega} \sum_{n_\tau=1}^{N_\tau} \left|R_{rec} - R_{exp}\right|}{N_\omega\, N_\tau}, \tag{25}$$

where n_ω and n_τ denote the sum over the N_ω and N_τ frequency and delay points of the experimental (R_{exp}) and reconstructed (R_{rec}) traces. Until the minimum set error or the maximum iteration number are not reached, the algorithm moves to the next iteration, starting back from the first delay point and updating object and probe in sequence.

Funding. Ministero dell'Istruzione, dell'Università e della Ricerca (MIUR) under the PRIN programme (2017RKWTMY, aSTAR, 20173B72NB); European Research Council Horizon 2020 Research and Innovation Programme (848411, AuDACE).

Disclosures. The authors declare no conflicts of interest.

Optics EXPRESS

Data availability. Data underlying the results presented in this paper are not publicly available at this time but may be obtained from the authors upon reasonable request.

References

1. S. Y. Kruchinin, F. Krausz, and V. S. Yakovlev, "Colloquium: Strong-field phenomena in periodic systems," Rev. Mod. Phys. **90**(2), 021002 (2018).
2. M. Volkov, S. A. Sato, F. Schlaepfer, L. Kasmi, N. Hartmann, M. Lucchini, L. Gallmann, A. Rubio, and U. Keller, "Attosecond screening dynamics mediated by electron localization in transition metals," Nat. Phys. **15**(11), 1145–1149 (2019).
3. F. Schlaepfer, M. Lucchini, S. A. Sato, M. Volkov, L. Kasmi, N. Hartmann, A. Rubio, L. Gallmann, and U. Keller, "Attosecond optical-field-enhanced carrier injection into the gaas conduction band," Nat. Phys. **14**(6), 560–564 (2018).
4. M. Schultze, K. Ramasesha, C. Pemmaraju, S. Sato, D. Whitmore, A. Gandman, J. S. Prell, L. J. Borja, D. Prendergast, K. Yabana, D. M. Neumark, and S. R. Leone, "Attosecond band-gap dynamics in silicon," Science **346**(6215), 1348–1352 (2014).
5. M. Zürch, H.-t. Chang, L. J. Borja, P. M. Kraus, S. K. Cushing, A. Gandman, C. J. Kaplan, M. H. Oh, J. S. Prell, D. Prendergast, C. D. Pemmaraju, D. M. Neumark, and S. R. Leone, "Direct and simultaneous observation of ultrafast electron and hole dynamics in germanium," Nat. Commun. **8**(1), 15734 (2017).
6. M. Zürch, H.-T. Chang, P. M. Kraus, S. K. Cushing, L. J. Borja, A. Gandman, C. J. Kaplan, M. H. Oh, J. S. Prell, D. Prendergast, C. D. Pemmaraju, D. M. Neumark, and S. R. Leone, "Ultrafast carrier thermalization and trapping in silicon-germanium alloy probed by extreme ultraviolet transient absorption spectroscopy," Struct. Dyn. **4**(4), 044029 (2017).
7. C. J. Kaplan, P. M. Kraus, A. D. Ross, M. Zürch, S. K. Cushing, M. F. Jager, H.-T. Chang, E. M. Gullikson, D. M. Neumark, and S. R. Leone, "Femtosecond tracking of carrier relaxation in germanium with extreme ultraviolet transient reflectivity," Phys. Rev. B **97**(20), 205202 (2018).
8. A. R. Attar, H.-T. Chang, A. Britz, X. Zhang, M.-F. Lin, A. Krishnamoorthy, T. Linker, D. Fritz, D. M. Neumark, R. K. Kalia, A. Nakano, P. Ajayan, P. Vashishta, U. Bergmann, and S. R. Leone, "Simultaneous Observation of Carrier-Specific Redistribution and Coherent Lattice Dynamics in 2H-$MoTe_2$ with Femtosecond Core-Level Spectroscopy," ACS Nano **14**(11), 15829–15840 (2020).
9. B. Buades, A. Picón, E. Berger, I. León, N. Di Palo, S. L. Cousin, C. Cocchi, E. Pellegrin, J. H. Martin, S. Ma nas-Valero, E. Coronado, T. Danz, C. Draxl, M. Uemoto, K. Yabana, M. Schultze, S. Wall, M. Zürch, and J. Biegert, "Attosecond state-resolved carrier motion in quantum materials probed by soft x-ray XANES," Appl. Phys. Rev. **8**(1), 011408 (2021).
10. M. Lucchini, S. A. Sato, A. Ludwig, J. Herrmann, M. Volkov, L. Kasmi, Y. Shinohara, K. Yabana, L. Gallmann, and U. Keller, "Attosecond dynamical franz-keldysh effect in polycrystalline diamond," Science **353**(6302), 916–919 (2016).
11. H. Mashiko, K. Oguri, T. Yamaguchi, A. Suda, and H. Gotoh, "Petahertz optical drive with wide-bandgap semiconductor," Nat. Phys. **12**(8), 741–745 (2016).
12. M. Schultze, E. M. Bothschafter, A. Sommer, S. Holzner, W. Schweinberger, M. Fiess, M. Hofstetter, R. Kienberger, V. Apalkov, V. S. Yakovlev, M. I. Stockman, and F. Krausz, "Controlling dielectrics with the electric field of light," Nature **493**(7430), 75–78 (2013).
13. H. Mashiko, Y. Chisuga, I. Katayama, K. Oguri, H. Masuda, J. Takeda, and H. Gotoh, "Multi-petahertz electron interference in cr: Al 2 o 3 solid-state material," Nat. Commun. **9**(1), 1468 (2018).
14. M. Lucchini, S. A. Sato, G. D. Lucarelli, B. Moio, G. Inzani, R. Borrego-Varillas, F. Frassetto, L. Poletto, H. Hübener, U. De Giovannini, A. Rubio, and M. Nisoli, "Unravelling the intertwined atomic and bulk nature of localised excitons by attosecond spectroscopy," Nat. Commun. **12**(1), 1021 (2021).
15. R. Geneaux, H. J. Marroux, A. Guggenmos, D. M. Neumark, and S. R. Leone, "Transient absorption spectroscopy using high harmonic generation: a review of ultrafast x-ray dynamics in molecules and solids," Phil. Trans. R. Soc. A **377**(2145), 20170463 (2019).
16. S. W. Koch, M. Kira, G. Khitrova, and H. M. Gibbs, "Semiconductor excitons in new light," Nat. Mater. **5**(7), 523–531 (2006).
17. G. D. Scholes and G. Rumbles, "Excitons in nanoscale systems," Nat. Mater. **5**(9), 683–696 (2006).
18. L. Butov, "Excitonic devices," Superlattices Microstruct. **108**, 2–26 (2017).
19. A. Moulet, J. B. Bertrand, T. Klostermann, A. Guggenmos, N. Karpowicz, and E. Goulielmakis, "Soft x-ray excitonics," Science **357**(6356), 1134–1138 (2017).
20. R. Géneaux, C. J. Kaplan, L. Yue, A. D. Ross, J. E. Baekhøj, P. M. Kraus, H.-t. Chang, A. Guggenmos, M.-y. Huang, M. Zürch, K. J. Schafer, D. M. Neumark, M. B. Gaarde, and S. R. Leone, "Attosecond Time-Domain Measurement of Core-Level-Exciton Decay in Magnesium Oxide," Phys. Rev. Lett. **124**(20), 207401 (2020).
21. J. Herrmann, M. Weger, R. Locher, M. Sabbar, P. Rivière, U. Saalmann, J.-M. Rost, L. Gallmann, and U. Keller, "Virtual single-photon transition interrupted: Time-gated optical gain and loss," Phys. Rev. A **88**(4), 043843 (2013).
22. L. Drescher, G. Reitsma, T. Witting, S. Patchkovskii, J. Mikosch, and M. J. J. Vrakking, "State-Resolved Probing of Attosecond Timescale Molecular Dipoles," J. Phys. Chem. Lett. **10**(2), 265–269 (2019).

Optics EXPRESS

23. L. Drescher, M. J. J. Vrakking, and J. Mikosch, "Attosecond transient absorption spectroscopy without inversion symmetry," J. Phys. B: At., Mol. Opt. Phys. **53**(16), 164005 (2020).
24. D. Spangenberg, P. Neethling, E. Rohwer, M. H. Brügmann, and T. Feurer, "Time-domain ptychography," Phys. Rev. A **91**(2), 021803 (2015).
25. D. Spangenberg, E. Rohwer, M. H. Brügmann, and T. Feurer, "Ptychographic ultrafast pulse reconstruction," Opt. Lett. **40**(6), 1002–1005 (2015).
26. M. Lucchini, M. Brügmann, A. Ludwig, L. Gallmann, U. Keller, and T. Feurer, "Ptychographic reconstruction of attosecond pulses," Opt. Express **23**(23), 29502–29513 (2015).
27. J. Itatani, F. Quéré, G. L. Yudin, M. Y. Ivanov, F. Krausz, and P. B. Corkum, "Attosecond streak camera," Phys. Rev. Lett. **88**(17), 173903 (2002).
28. F. Novelli, D. Fausti, F. Giusti, F. Parmigiani, and M. Hoffmann, "Mixed regime of light-matter interaction revealed by phase sensitive measurements of the dynamical Franz-Keldysh effect," Sci. Rep. **3**(1), 1227 (2013).
29. A. Mysyrowicz, D. Hulin, A. Antonetti, A. Migus, W. T. Masselink, and H. Morkoc, ""dressed excitons" in a multiple-quantum-well structure: evidence for an optical stark effect with femtosecond response time," Phys. Rev. Lett. **56**(25), 2748–2751 (1986).
30. G. Mahan, "Emission spectra and phonon relaxation," Phys. Rev. B **15**(10), 4587–4595 (1977).
31. A. Wirth, M. T. Hassan, I. Grguraš, J. Gagnon, A. Moulet, T. T. Luu, S. Pabst, R. Santra, Z. A. Alahmed, A. M. Azzeer, V. S. Yakovlev, V. Pervak, F. Krausz, and E. Goulielmakis, "Synthesized Light Transients," Science **334**(6053), 195–200 (2011).
32. N. B. Delone and V. P. Krainov, "Ac stark shift of atomic energy levels," Phys.-Usp. **42**(7), 669–687 (1999).
33. C. Cirelli, M. Sabbar, S. Heuser, R. Boge, M. Lucchini, L. Gallmann, and U. Keller, "Energy-Dependent Photoemission Time Delays of Noble Gas Atoms Using Coincidence Attosecond Streaking," IEEE J. Sel. Top. Quantum Electron. **21**(5), 1–7 (2015).
34. T. Gaumnitz, A. Jain, and H. J. Wörner, "Complete reconstruction of ultra-broadband isolated attosecond pulses including partial averaging over the angular distribution," Opt. Express **26**(11), 14719 (2018).
35. C. Bourassin-Bouchet, L. Barreau, V. Gruson, J.-F. Hergott, F. Quéré, P. Salières, and T. Ruchon, "Quantifying Decoherence in Attosecond Metrology," Phys. Rev. X **10**(3), 031048 (2020).
36. R. Almairac and C. Benoit, "Lattice dynamics of magnesium fluoride," J. Phys. C: Solid State Phys. **7**(15), 2614–2629 (1974).
37. B. McCallum and J. Rodenburg, "Two-dimensional demonstration of Wigner phase-retrieval microscopy in the STEM configuration," Ultramicroscopy **45**(3-4), 371–380 (1992).
38. P. Thibault, M. Dierolf, O. Bunk, A. Menzel, and F. Pfeiffer, "Probe retrieval in ptychographic coherent diffractive imaging," Ultramicroscopy **109**(4), 338–343 (2009).
39. A. M. Maiden and J. M. Rodenburg, "An improved ptychographical phase retrieval algorithm for diffractive imaging," Ultramicroscopy **109**(10), 1256–1262 (2009).
40. A. Maiden, D. Johnson, and P. Li, "Further improvements to the ptychographical iterative engine," Optica **4**(7), 736–745 (2017).
41. J. Musfeldt, D. Tanner, and A. Paine, "Method for the determination of the optical properties of highly conjugated pigments," J. Opt. Soc. Am. A **10**(12), 2648–2657 (1993).
42. G. D. Lucarelli, B. Moio, G. Inzani, N. Fabris, L. Moscardi, F. Frassetto, L. Poletto, M. Nisoli, and M. Lucchini, "Novel beamline for attosecond transient reflection spectroscopy in a sequential two-foci geometry," Rev. Sci. Instrum. **91**(5), 053002 (2020).
43. D. J. Kane and R. Trebino, "Characterization of arbitrary femtosecond pulses using frequency-resolved optical gating," IEEE J. Quantum Electron. **29**(2), 571–579 (1993).
44. C. Iaconis and I. A. Walmsley, "Spectral phase interferometry for direct electric-field reconstruction of ultrashort optical pulses," Opt. Lett. **23**(10), 792–794 (1998).
45. P. D. Keathley, S. Bhardwaj, J. Moses, G. Laurent, and F. X. Kärtner, "Volkov transform generalized projection algorithm for attosecond pulse characterization," New J. Phys. **18**(7), 073009 (2016).
46. R. Géneaux, H.-T. Chang, A. M. Schwartzberg, and H. J. B. Marroux, "Source noise suppression in attosecond transient absorption spectroscopy by edge-pixel referencing," Opt. Express **29**(2), 951–960 (2021).
47. M. Lucchini, G. D. Lucarelli, M. Murari, A. Trabattoni, N. Fabris, F. Frassetto, S. De Silvestri, L. Poletto, and M. Nisoli, "Few-femtosecond extreme-ultraviolet pulses fully reconstructed by a ptychographic technique," Opt. Express **26**(6), 6771 (2018).
48. M. Murari, G. D. Lucarelli, M. Lucchini, and M. Nisoli, "Robustness of the ePIE algorithm for the complete characterization of femtosecond, extreme ultra-violet pulses," Opt. Express **28**(7), 10210 (2020).